Results in Physics 9 (2018) 1391–1402

Contents lists available at ScienceDirect

Results in Physics

journal homepage: www.elsevier.com/locate/rinp

Nanostructured stannic oxide: Synthesis and characterisation for potential energy storage applications

D. Dodoo-Arhin[a,b,*], R.A. Nuamah[a,b], P.K. Jain[b,c], D.O. Obada[d], A. Yaya[a]

[a] Department of Materials Science and Engineering, University of the Ghana, Ghana
[b] African Materials Science and Engineering Network (A Carnegie-IAS RISE Network), South Africa
[c] Department of Physics, University of Botswana, Botswana
[d] Department of Mechanical Engineering, Ahmadu Bello University, Zaria, Nigeria

ARTICLE INFO

Keywords:
SnO_2 nanoparticles
Supercapacitor
Hydrothermal technique
Cyclic voltammetry

ABSTRACT

SnO_2 nanoparticles were synthesized using the hydrothermal technique. Well crystalline particles with different morphologies and crystallite size in the range of 2 nm–10 nm were obtained by using Urea and Soduim Borohydride as reducing agents, and deploying Dioctyl Sulfosuccinate Sodium Salt (**AOT**) and Cetyl Trimethyl ammonium bromide (**CTAB**) as the surfactants. Samples have been characterised by X-ray diffraction, Scanning Electron microscopy, Energy Dispersive X-ray spectroscopy, specific surface area, porosity, and Fourier Transform Infrared spectroscopy. Preliminary studies on the potential electrochemical properties of the as-produced nanoparticles were investigated using cyclic voltammetry, electrochemical impedance spectroscopy and potentiostatic charge-discharge in aqueous KOH electrolyte. The surfactant and reducing agents used in the synthesis procedure of SnO_2 nanoparticles influenced the particle size and the morphology, which in turn influenced the capacitance of the SnO_2 nanoparticles. The SnO_2 electrode material showed pseudocapacitor properties with a maximum capacitance value of 1.6 Fg^{-1} at a scan rate of 5 mVs^{-1}, an efficiency of 52% at a current of 1 mA and a maximum capacitance retention of about 40% after 10 cycles at a current of 1 mA. From the Nyquist plot, The ESR for the samples increase accordingly as SCA (31.5 Ω) < SAA (31.85 Ω) < SE (36.3 Ω) < SAT (36.92 Ω) < SCT (40.41 Ω) < SA < SC (53.97 Ω). These values are a confirmation of the low capacitance, efficiencies and capacitance retention recorded. The results obtained demonstrate the potential electrochemical storage applications of SnO_2 nanoparticles without the addition of conductive materials.

Introduction

For some time now, considerable efforts have been made to develop new energy storage devices which have high energy and high power density to meet the world's demand for clean energy. Supercapacitors (SCs) which are also known as Electrochemical Capacitors (ECs) are promising energy storage devices. They can produce a large amount of energy in a short period of time and they are usually preferred for energy storage systems due to their excellent cyclability and very good power performance as compared to conventional capacitors and batteries [1]. Supercapacitors are currently used in a wide range of consumer electronics, memory back-up systems, and industrial power and energy management. A new development as far as supercapacitors are concerned is their use in emergency doors on Airbus A380. Another promising application is their use in low-emission hybrid electric vehicles and fuel cell vehicles to serve as a temporary energy storage device with a high-power capability to store energies when braking. Supercapacitors can be grouped into two types (Electrical Double Layer Capacitor and Pseudocapacitor) according to their charge/discharge mechanisms [2]. The Electrical Double Layer Capacitor stores energy by electrostatic adsorption/desorption between polarized solid electrode vertical line liquid electrolyte interfaces, and the Pseudocapacitor stores energy by surface faradaic redox reactions on the interface of the electroactive material and the electrolyte. The large capacitance of the Pseudocapacitor is made possible by electrode material that can be reversibly oxidized and reduced over a wide potential range [2–4].

The major electrode materials that are used in supercapacitors are those made of graphene and other carbonaceous materials (carbon nanotubes, activated carbon, etc.). The desire to use carbon materials comes from the fact that they store the charges electrostatically using reversible adsorption of ions of the electrolyte onto active materials that are electrochemically stable and have a high accessible surface area. However, their low specific charge has made scientists look into finding new materials which are environmentally friendly and have high

* Corresponding author at: Department of Materials Science and Engineering, University of the Ghana, Ghana.
E-mail address: ddodoo-arhin@ug.edu.gh (D. Dodoo-Arhin).

https://doi.org/10.1016/j.rinp.2018.04.057
Received 17 January 2018; Received in revised form 9 April 2018; Accepted 20 April 2018
Available online 28 April 2018

Table 1
Experimental Parameters.

Sample Id	Method	$SnCl_2{\cdot}2H_2O$ (g)	Reducing Agent	pH	Domain Size (nm)	BET surface Area (m^2/g)	Pore Size (Å)	Pore volume cm^3/g
SA	$SnCl_2{\cdot}2H_2O$ + $NaBH_4$	2.1	2.6 g $NaBH_4$	9.03	2.5	88.3118	114.9269	0.253735
SAA	$SnCl_2{\cdot}2H_2O$ + $NaBH_4$ + AOT	2.1	2.6 g $NaBH_4$	9.18	3.1	63.9505	157.1270	0.251209
SAT	$SnCl_2{\cdot}2H_2O$ + $NaBH_4$ + CTAB	2.1	2.6 g $NaBH_4$	8.94	6.1	54.9821	126.0116	0.173210
SC	$SnCl_2{\cdot}2H_2O$ + Urea	2.1	2.6 g Urea	8.27	10.5	50.9202	173.9906	0.232929
SCA	$SnCl_2{\cdot}2H_2O$ + Urea + AOT	2.1	2.6 g Urea	8.42	6.2	26.6186	210.4345	0.140037
SCT	$SnCl_2{\cdot}2H_2O$ + Urea + CTAB	2.1	2.6 g Urea	8.12	11.5.	18.6892	23.1262	0.010805

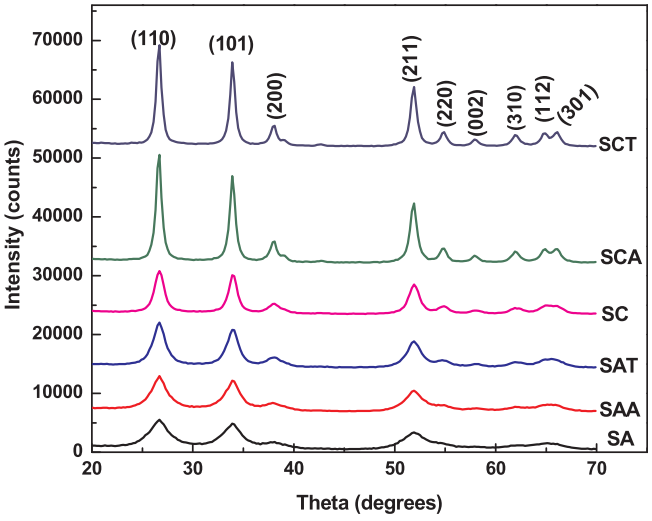

Fig. 1a. XRD patterns of SnO_2 nanoparticles.

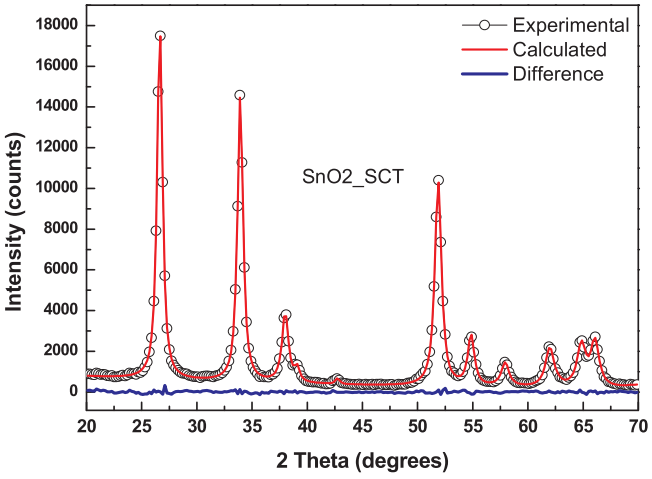

Fig. 1b. SnO_2-SCT modelled using WPPM.

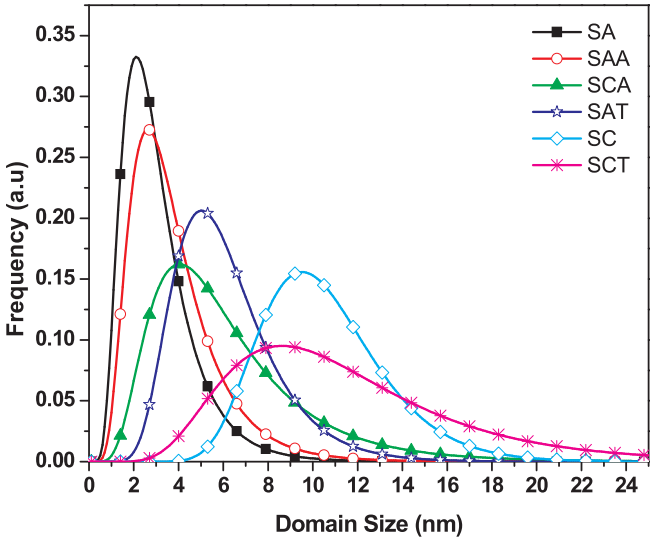

Fig. 1c. Lognormal Size Distribution Analysis of the SnO_2 particles.

energy storage capacity [5]. Transition metal oxides have also been studied widely for use as electrode materials for supercapacitors. Although RuO_2 has good capacitive properties as a supercapacitor electrode material (specific capacitance: 1300 Fg^{-1}) [6], its toxic nature, rarity and high production cost will exclude it from wide and commercial applications. Manganese oxide is another transition metal oxide studied as an electrode material for supercapacitor application. Manganese can exist in three different valence states and its oxides are highly complex. Theoretically, the capacitance of manganese oxides is estimated to be up 1100 Cg^{-1} (from Mn (IV) to Mn (III)) but the electrochemical reversibility of redox transition of manganese dioxide is usually too low to be applicable, and pure manganese dioxide possesses a poor capacitive response due to the high resistance of bulk manganese oxide [7].

Tin oxide (SnO_2), a transparent conducting oxide and a wide band gap n-type semiconductor, has been used in many applications such as gas sensors [8], electrodes in solid-state ionic devices [9], solar cells [10], etc., due to its unique properties such as its being chemically inert, mechanically hard, and thermally stable. Only one stable phase (there is no metastable one) is known, which has a tetragonal arrangement of the atoms exhibiting either a rutile or cassiterite structure [11]. Tin oxide can be synthesized using a variety of techniques such as sol-gel [12], the hydrothermal method [13], precipitation [14], spray pyrolysis [15] and Chemical Vapour Deposition [16]. Techniques such as precipitation provide particle sizes of less surface area and smaller pore size as a result of agglomeration, which makes them unsuitable for applications such as gas sensors and electrode materials for supercapacitors and batteries as compared to hydrothermal and microemulsions techniques [17–19].

In this paper tin oxide nanoparticles were synthesized via the hydrothermal technique under mild conditions (120 °C) using sodium borohydride and urea as the reducing agents. Physical and electrochemical characterizations were performed on the tin oxide nanoparticles using X-ray Diffraction (XRD), Fourier Transform Infrared Spectroscopy, Energy Dispersive Spectroscopy, Scanning Electron Microscopy, and Cyclic Voltammetry to determine the phase, surface morphology, chemical bonds and charge and discharge properties of the as-synthesized tin oxide particles. This is with a view of exploring the potential of SnO_2 nanoparticles for energy storage applications.

Experimental

Materials and chemicals

All the reagents used in this work were of analytical grade and were

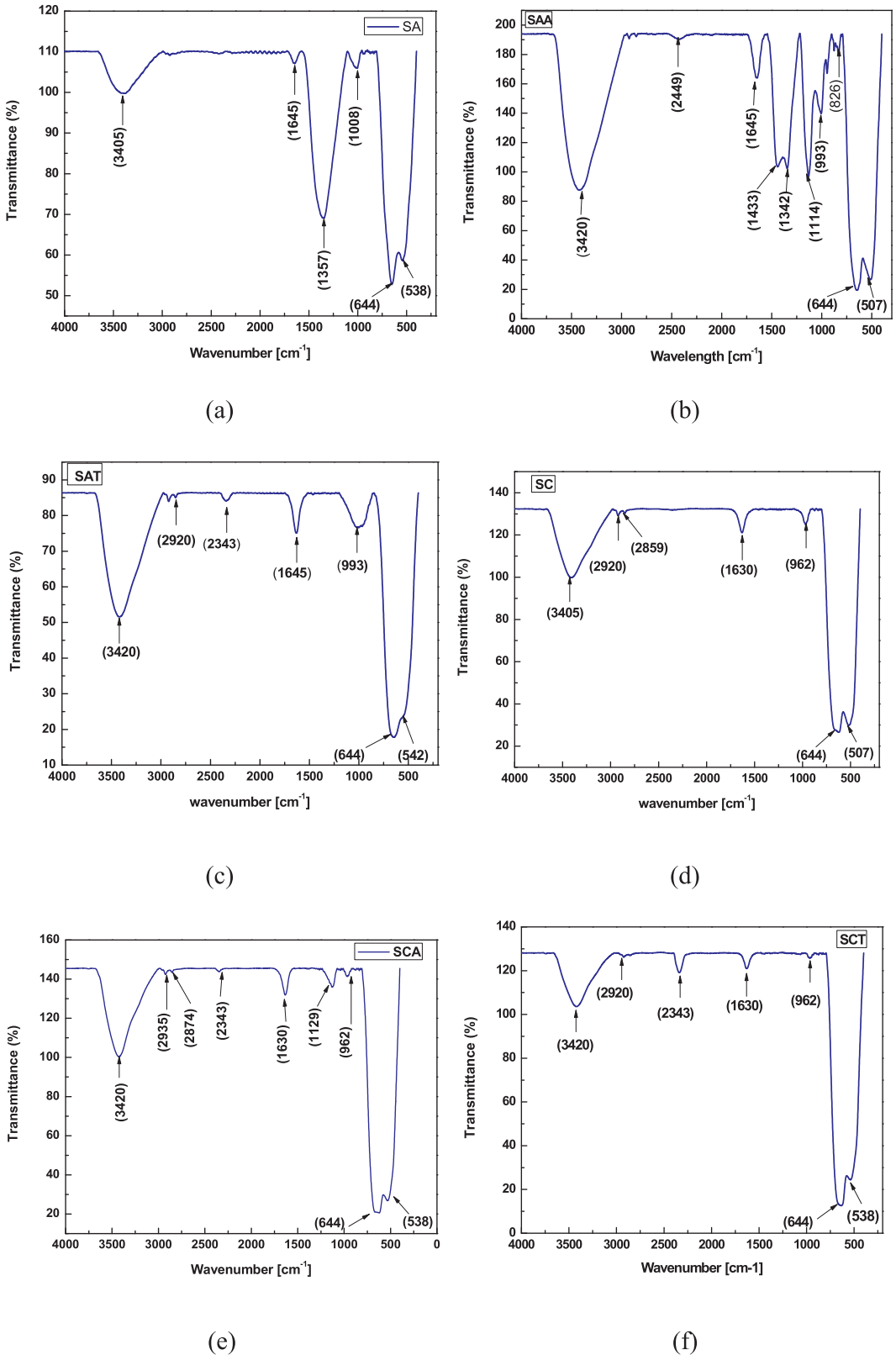

Fig. 2. FTIR spectra of as-synthesized SnO_2 nanoparticles: (a) SA, (b) SAA; (c) SAT, (d) SC; (e) SCA (f) SCT.

used without any further purification. The reagents and materials used include Tin (IV) Chloride pentahydrate ($SnCl_4{\cdot}5H_2O$), [98% Sigma Aldrich], Urea ($CO(NH_2)_2$), [Paskem]; Sodium Borohydride ($NaBH_4$) [Lab. Tech chemicals]; Ethanol (C_2H_5OH), [96%, BDH laboratory supplies (Analar)]; distilled water; Dioctyl Sulfosuccinate sodium salt (AOT, $C_{20}H_{37}NaO_7S$) [Sigma Aldrich]; Cetyl Trimethyl ammonium bromide (CTAB, $C_{19}H_{42}BrN$), [Central Drug House Ltd]; Nickel foam [Alantum-korea]; polyvinylidene difluoride (PVdF) [Sigma Aldrich]; 1-methyl-2-pyrrolidinone (NMP) [Sigma Aldrich].

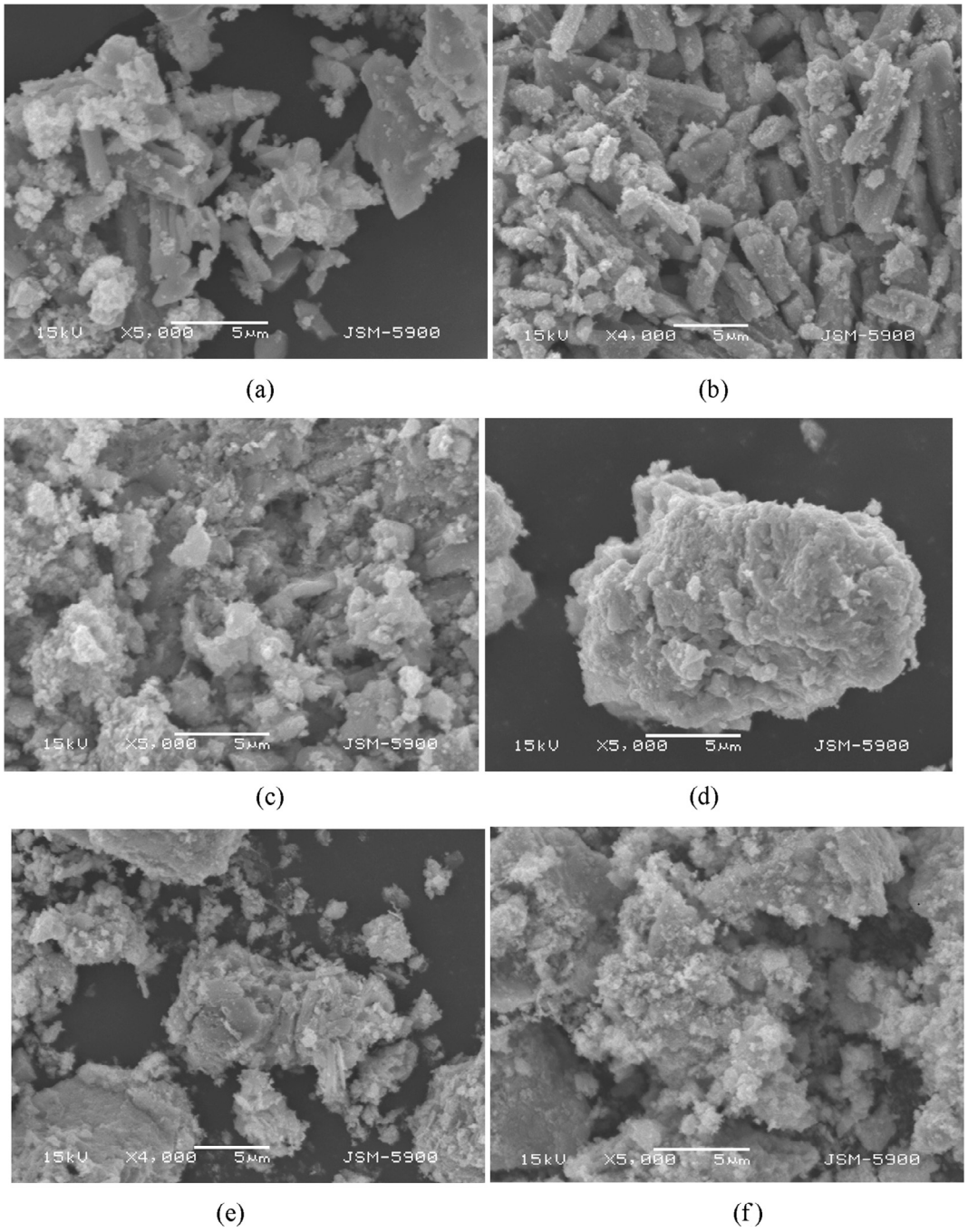

Fig. 3. SEM Micrographs of SnO_2 nanoparticles of the various treatments – (a) SA, (b) SAA, (c) SAT, (d) SC, (e) SCA, (f) SCT.

Synthesis of SnO_2 nanoparticles

In a typical hydrothermal synthesis of the nanoparticles (see Table 1), 2.1 g of $SnCl_4{\cdot}5H_2O$ was added to a solution consisting of 60 ml of water and 60 ml ethanol under constant stirring at room temperature. 2.6 g of urea was then added drop-wise to the colourless mixture under rigorous stirring for 15mins and the pH of the solution determined. The greenish brown mixture was subsequently transferred into a 200 ml Teflon-lined steel autoclave and heated at 120 °C for 7 h at a vessel pressure of 15psi to complete the hydrothermal reaction. After autoclaving, the white precipitates from the precursor solution were washed several times with distilled water and ethanol via a centrifugation process to rid the precipitates of any impurity. The washed precipitates were then dried overnight in an oven at 100 °C, after which the dried precipitates were calcined in a Linn High therm electric furnace at 600 °C for 3 h. The reaction mechanism is represented by the Eqs. (16). The final product was stored for further characterization. The procedure was repeated for both the surfactant template assisted and non-surfactant assisted hydrothermal processes.

Pretreatment of the Nickel foam substrate

The Nickel foam substrate was carefully etched with hydrochloric acid (HCl 2 M) for thirty minutes to ensure the removal of NiO layer on the surface. The etched Ni substrate was then rinsed in ethanol and distilled water several times via an ultrasonic cleaner.

Preparation of the SnO_2 Working Electrodes. The working electrodes for electrochemical evaluation were prepared by mixing 98 wt% of SnO_2 nanoparticles from the various treatments and 2 wt% polyvinylidene difluoride (PVdF) binder in a mortar. The mixture was then

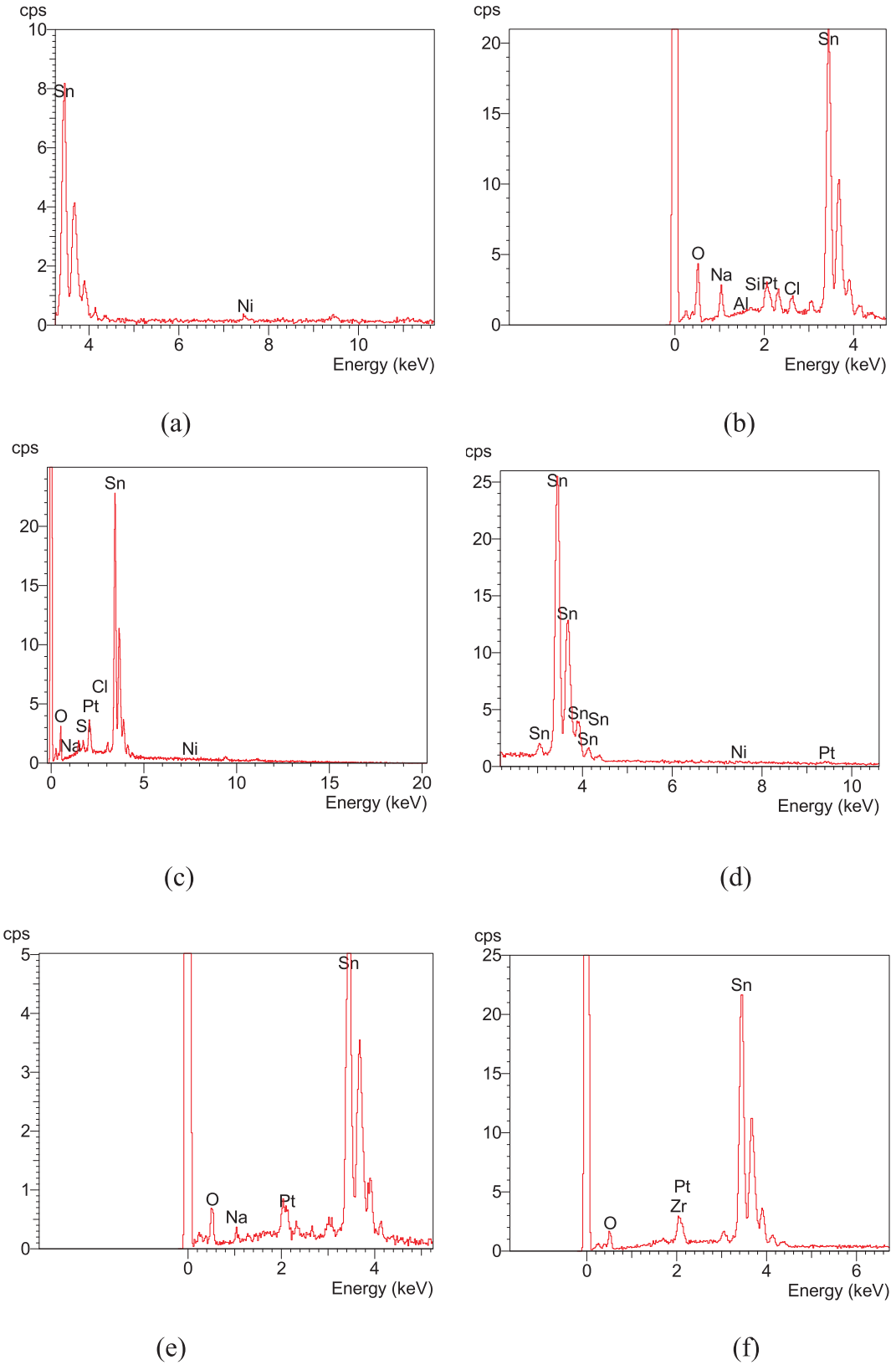

Fig. 4. EDX spectra of SnO_2 nanoparticles under the various treatments – (a) SA, (b) SAA, (c) SAT, (d) SC, (e) SCA, (f) SCT.

dissolved in 1-methyl-2-pyrrolidinone (NMP) to form a slurry. The slurry was coated on the treated Ni foam with dimensions 3 cm × 1 cm and pore size of 450 μm and dried overnight at 80 °C to ensure complete evaporation of the NMP.

Characterization of SnO_2 nanoparticles

The as-produced nanoparticles are then characterized via X-ray Diffraction (XRD), Scanning Electron Microscopy (SEM), Fourier

Table 2
EDX atomic % of the synthesized SnO_2 nanoparticles.

Sample	Element (Atomic %)		Atomic ratio of Sn:O
	O	Sn	
SA	66.29	30.21	1:1.19
SAA	54.95	30.33	1:1.81
SAT	63.31	33.04	1:1.92
SC	81.06	61.54	1:1.32
SCA	58.37	36.45	1:1.60
SCT	76.46	21.51	1:3.55

Transform Infra-Red (FTIR), and *Brunauer–Emmett–Teller* (*BET*) surface area analysis for their crystal structure, optical, microstructure, porosity and surface properties. To determine the phases present and the microstructure of the SnO_2 nanoparticles, X-ray powder diffraction (XRD) patterns were collected on an Empyrean diffractometer (Panalytical BV, Netherlands) with theta/theta geometry, operating a Cu Kα radiation tube (λ = 1.5418 Å) at 40 kV and 45 mA. The XRD patterns of all the randomly oriented powder specimens were recorded in the 20°–70° 2θ range with a step size of 0.017° and a counting time of 14 s per step. The diffraction patterns were matched against the ICSD's PDF database and qualitative phase analysis conducted using the X'Pert Highscore plus search match software (Panalytical, Netherlands). The instrumental resolution function was characterized with the NIST SRM 640d (Si) standard [20] and all peak profiles were simultaneously fitted with symmetrical pseudo-Voigt functions whose width and shape were constrained according to the Caglioti formulae [21]. Microstructural analysis was performed using the Whole Powder Pattern Modelling (WPPM) method [22], with the aid of the PM2K software [23].

A high resolution JSM5900 scanning electron microscope operated at 2.0 kV was used in the surface morphological investigations of the as-produced particles. Prior to the SEM analysis, the samples were metallized with carbon coating to render them conductive.

Specific surface area (SSA) and porosity of the synthesized powders were measured by nitrogen chemisorption using an Accelerated Surface Area and Porosimetry System, model ASAP 2010 (Micromeritics Instrument Corporation). In the BET/porosity characterization, the samples (≈0.2 g) were outgassed at 300 °C in a vacuum for 24 h. The data of the adsorption and desorption isotherms were used to evaluate the porosity of the sample. Transmission FTIR spectra were recorded on a Vertex 70 v (Bruker) spectrometer in the 4000–400 cm^{-1} range with a 4 cm^{-1} resolution. Sample compartment was evacuated during acquisition and the contact between the sample and the diamond ATR crystal was of 2 mm diameter. Spectra were recorded and analysed with the Opus software.

Results and discussion

Synthesis

Tin (IV) chloride molecules are known to adopt a near perfect tetrahedral symmetry with average Sn-Cl distance of 227.9 pm. In aqueous solutions, $SnCl_4$ dissociates into $[Sn(H_2O)_6]^{4+}$ ions and Cl^- anions that can partially coordinate with the Tin (Sn^{4+}) ions. In $[Sn(H_2O)_6]^{4+}$, the six water molecules completely surround the Sn^{4+} providing a shielding effect. The addition of $NaBH_4$ to the water-ethanol-precursor solution, causes the following reaction to occur:

$$NaBH_{4(s)} + 2H_2O_{(l)} \rightarrow NaBO_{2(aq)} + 4H_{2(g)} + \text{heat} \quad (1)$$

The interaction of the produced hydrogen gas with the dissolved hydroxyl ions generates solvated electrons:

$$H_{2(g)} + 2OH^-_{(aq)} \rightarrow 2H_2O_{(aq)} + 2e^-_{(aq)} \quad (2)$$

The solvated electrons can penetrate the hexaaquaTin(IV) ions system reducing it to $Sn^{4+}(H_2O)_x$ (x = 1–4) ions. The excess of OH^- ions from the ethanol contribution and at temperature higher than room temperature, SnO_2 can be form through the following scheme:

$$Sn^{4+}_{(aq)} + Cl^- + C_2H_5^+4OH^-_{(aq)} \rightarrow Sn(OH)^{2-}_{4(aq)} + C_2H_5Cl_{(aq)} \quad (3)$$

The dissolved C_2H_4Cl impurities are removed by washing with a 1:1 water –ethanol solution. The resultant Tin hydroxide is then oven dried and then calcined:

$$Sn(OH)^{2-}_{4(aq)} \xrightarrow{\text{Heat}} SnO_{2(s)} + 2H_2O_{(2)} \quad (4)$$

The reaction equation for the precursor solution using urea as reducing agent is shown as:

$$CO(NH_2)_{2(S)} + 3H_2\ O \rightarrow CO_{2(g)} + 2NH_4^+ + 2OH^- \quad (5)$$

$$Sn^{4+}_{(aq)} + Cl^- + NH_4^+ + 4OH^-_{(aq)} \rightarrow Sn(OH)^{2-}_{4(aq)} + 2NH_4Cl_{(aq)} \quad (6)$$

The final product is washed with a 1:1 water –ethanol solution via centrifugation and decantation procedures to remove the dissolved NH_4Cl impurities. The resultant Tin hydroxide is then oven dried and then calcined as shown in Eq. (4).

The surfactant assisted systems are frequently used to control nucleation and growth of inorganic particles [24–25]. In this approach, the CTAB and AOT surfactant templates simply served as scaffolds with or around which the inorganic particles are generated in situ and shaped into nanostructures with its morphology complementary to that of the template. In this case of the as-prepared SnO_2 nanoparticles, the surfactant templates resulted in nanorod and nanoflower-like structures as shown in Fig. 3. From Table 1 it is observed that when sodium borohydride was used as the reducing agent (samples SA, SAA, SAT), the pH was higher than when urea was used as the reducing agent (samples SC, SCA, SCT). It can also be observed that the addition of CTAB to both sodium borohydride and urea precursor solutions (samples SAT, SCT) decreased the pH and this could be attributed to the fact that CTAB in aqueous solution dissociates to produce NH_4^+ ions which consume OH^- ions in the aqueous medium. Hence, there is OH^- deficiency and more H^+ in solution; leading to a decrease in pH.

X-ray diffraction analysis (XRD)

The diffraction peaks in Fig. 1a are markedly broadened, which indicates that the crystalline domain sizes of samples are very small, with the average size estimated from the WPPM (Fig. 1c) are in the range of being 2.5 nm–11.5 nm (see Table 1. It can be seen from the XRD data that samples produced with sodium borohydride (SA, SAA and SAT) have broader and less intense peaks than samples produced with urea (SC, SCA and SCT), which means that the samples produced with sodium borohydride have smaller crystallite sizes than particles produced with urea. This can be attributed to the fact that samples produced with sodium borohydride have a higher pH than samples produced with urea, and the higher the pH, the smaller the particles sizes [26]. In higher pH value solutions, the coordinated water molecules suppress the agglomeration among the freshly formed nanocrystallites [26–27]. The Whole Powder Pattern Modelling (WPPM) approach using the PM2K software which connects a physical model for the microstructure with the diffraction pattern, allowing an extraction of the microstructure parameters without recurring arbitrary peak shapes to fit each diffraction peak, was used for the microstructure analysis. A typical diffraction pattern of sample SCT modelled with the WPPM is shown in Fig. 1b. The modelling was carried out by assuming the presence of a lognormal distribution (Fig. 1c) of aligned spherical domains. The almost featureless nature of the residual line in Fig. 1b indicates a good agreement between experimental data and model, which also suggests that the shape assumption is right for the domains investigated.

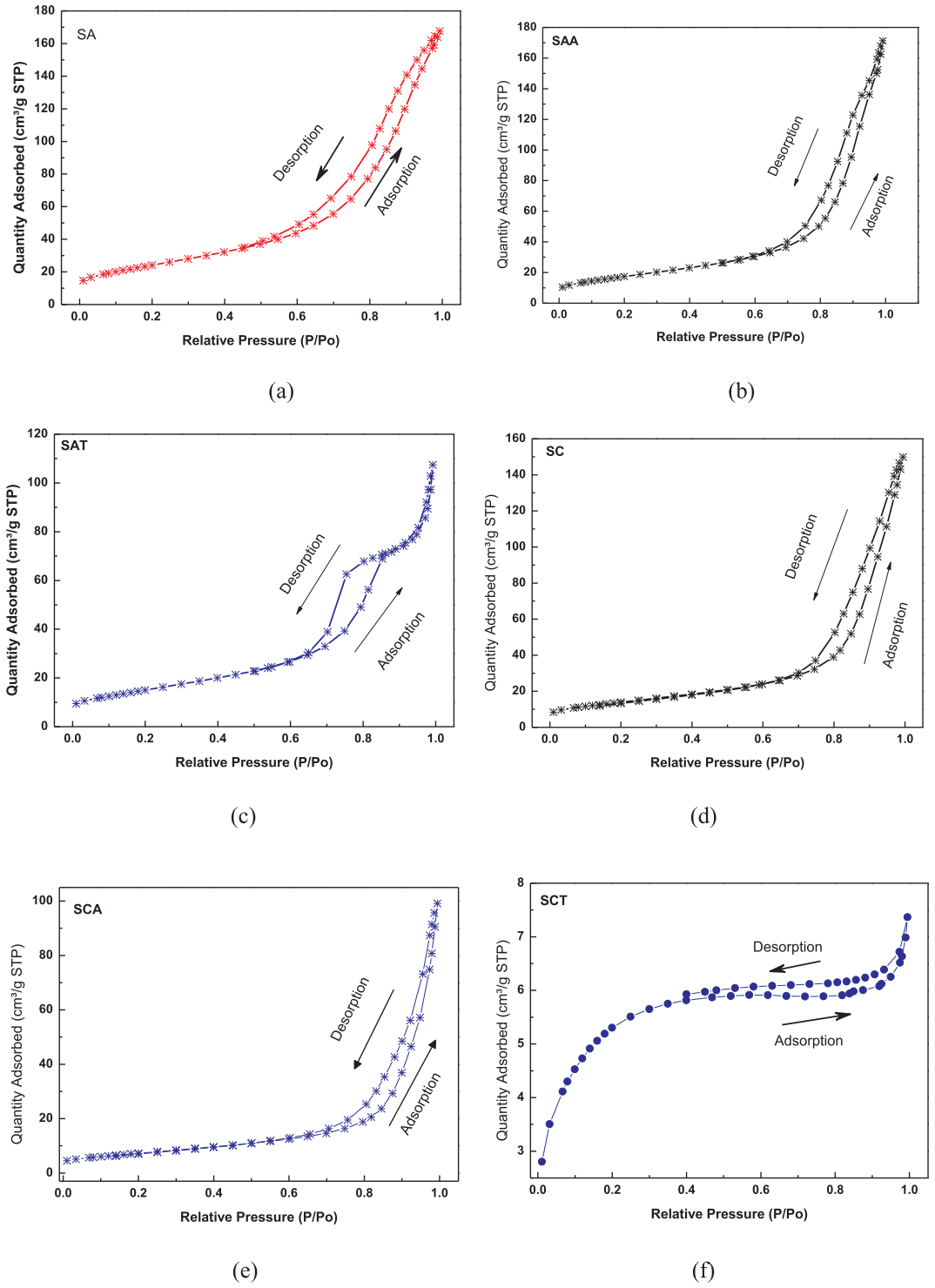

Fig. 5. Linear Isotherm plots of the as-synthesized SnO_2 nanoparticles; (a) SA, (b) SAA, (c) SAT, (d) SC, (e) SCA, (f) SCT.

Fourier Transform Infrared spectroscopy analysis (FTIR)

The FTIR results in Fig. 2(a–f) indicate that synthesized powder is tin oxide containing some degree of moisture (possibly crystallized water), residual hydroxide and some AOT content. Residual hydroxide content is an indication of either incomplete conversion of hydrated tin oxide or some reaction between SnO_2 and H_2O due to very high surface area (see Fig. 4 and Table 1 of the synthesized powder and the residual AOT from inadequate washing of precipitates before drying [28].

The peaks occurring at about 507 cm^{-1}–1357 cm^{-1} in Fig. 2(a–f) are attributed to Sn–O stretching modes of Sn–O–Sn and Sn–OH [29]. The peak at about 1630 cm^{-1}–1645 cm^{-1} belongs to H-OH bonds coming from the moisture content of the powders and the peak at 3405 cm^{-1} and 3420 cm^{-1} is attributed to Sn-OH bonds [30]. Peaks at about 2920–2949 cm^{-1} can also be attributed to hydroxyl groups that are absorbed on the Tin Oxide surface. There are no impurity peaks from the surfactant used, which together the XRD data confirms that phase pure SnO_2 nanoparticles were synthesized using the water-in oil microemulsions technique.

Fig. 2a represents the FTIR spectra of SnO_2 particles prepared using

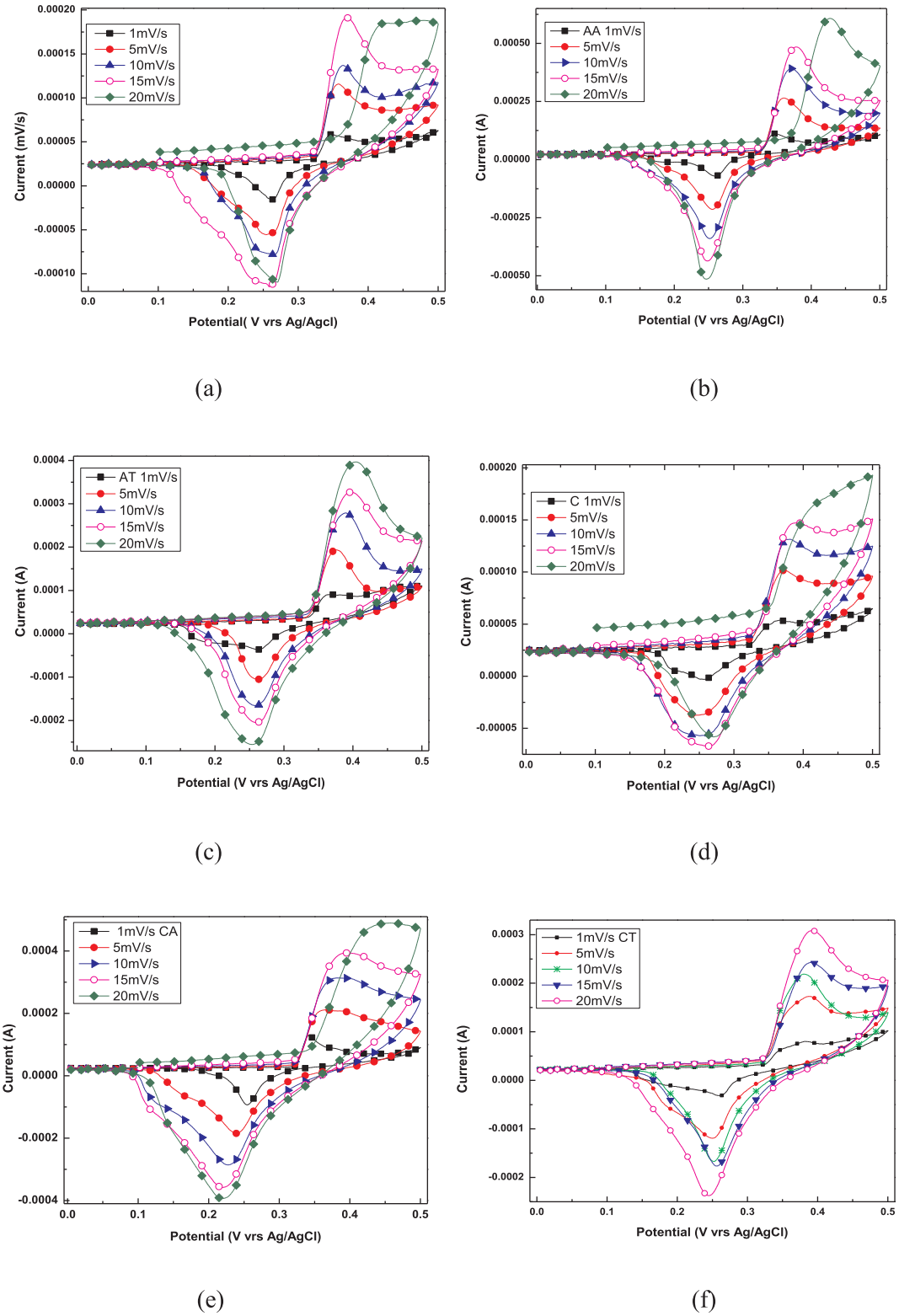

Fig. 6. Cyclic Voltagrams of the as-obtained SnO_2 nanoparticles at different scan rates – (a) SA; (b) SAA; (c) SAT; (d) SC; (e) SCA; (f) SCT.

sodium borohydride as a reducing agent. The peak at 3405 cm^{-1} is attributed to Sn-OH bonds. Peaks at 1008 cm^{-1}, 644 cm^{-1} and 538 cm^{-1} are attributed to Sn–O stretching modes of Sn–O–Sn and Sn–OH. Peak at 1645 cm^{-1} and 1357 cm^{-1} are attributed to H-OH bonds coming from the moisture content of the powder and Sn-OH bonds respectively.

The hydrophobic group R-SO_3 Na^+ of AOT is responsible for the peak at 993 cm^{-1} and 1114 cm^{-1}. From the above result (Fig. 2b), it is obvious that AOT molecules are adsorbed in the pores of the powders [31]. 2449 cm^{-1}, 3420 cm^{-1} and 1342 cm^{-1} peaks are attributed to Sn-OH bonds [30]. Peak at 1645 cm^{-1} is also assigned to H-OH bonds from the moisture content of the powder. 1433 cm^{-1} peak corresponds to bending vibrations of –CH_2. Which shows that a few organic groups are absorbed on the surfaces of SnO_2 nanoparticles [32] which could be

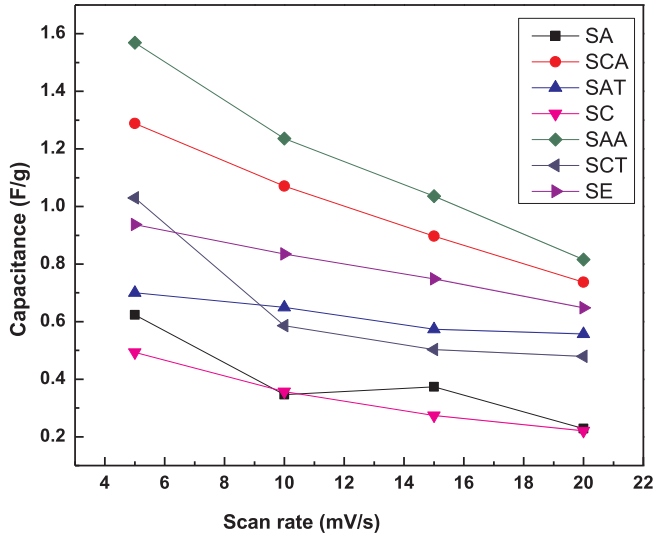

Fig. 7. Specific capacitance of the synthesized SnO_2 particles.

as a result of combustion of the organic groups.

From the Fig. 2c, the peak at 2920 cm^{-1} can be attributed to CH stretching [33]. The peak at 3420 cm^{-1}, 1645 cm^{-1} and 993 cm^{-1} are assigned to Sn-OH bonds, H-OH bonds from the moisture content of the powder and the hydrophobic group R-SO_3 Na^+ of AOT respectively [34]. 644 cm^{-1} 542 cm^{-1} peaks are attributed to Sn–O stretching modes of Sn–O–Sn.

The peaks at 3405 cm^{-1}, 1630 cm^{-1} and 962 cm^{-1} in the Fig. 2d are assigned to Sn-OH bonds, H-OH bonds from the moisture content of the powder. 2920 cm^{-1} and 2859 cm^{-1} are attributed to alkyl CH stretching [34]. 644 cm^{-1} and 507 cm^{-1} are attributed to Sn–O stretching modes of Sn–O–Sn and Sn–OH, respectively [29,35].

From Fig. 2e, peaks at 644 cm^{-1} and 538 cm^{-1} are attributed to Sn–O stretching modes of Sn–O–Sn and Sn–OH, respectively. 2935 cm^{-1} and 2874 cm^{-1} are attributed to alkyl CH stretching. The peak at 3420 cm^{-1}, 2343 cm^{-1}, 1630 cm^{-1} and 962 cm^{-1} are assigned to Sn-OH bonds, H-OH bonds from the moisture content of the powder [30].

From Fig. 2f, the peaks at 644 cm^{-1} and 538 cm^{-1} are attributed to Sn–O stretching modes of Sn–O–Sn and Sn–OH, respectively. 2935 cm^{-1} and 2874 cm^{-1} peaks are attributed to alkyl CH stretching. The peak at 3420 cm^{-1}, 2343 cm^{-1}, 1630 cm^{-1} and 962 cm^{-1} are assigned to Sn-OH bonds, H-OH bonds from the moisture content of the powder [30].

SEM micrographs of the as-synthesized SnO_2 nanoparticles

The SEM micrographs in Fig. 3 clearly show different morphologies for SnO_2 prepared in different surfactants. The shape of the agglomerated sample SC looked like florets of cauliflower (nanoflower-like structures). Nanorods were formed for samples SA and SAA. For samples prepared with CTAB (SCT and SAT), agglomerated particles were formed and this is because, in an aqueous system, CTAB ionizes completely and results in cation with a tetrahedral structure. The electrostatic interaction takes place between CTA^+ cations and $Sn(OH)_6^{2-}$ anions, the CTA^+ cations condense into aggregates in which counter ions $Sn(OH)_6^{2-}$ are interrelated in the interfaces between the head group to form CTA^+ – $Sn(OH)_6^{2-}$ pair [19,36]. AOT being an anionic surfactant, it was found that there is no direct interaction between the $Sn(OH)_6^{2-}$ ions and the SO_7^- head of the AOT since both are similarly charged. Both the $Sn(OH)_6^{2-}$ nanoparticles and micelles coexist individually with no significant change in the structure of the micelles [37]. The different morphology reveals the role of individual reducing agents and surfactants in controlling the nucleation and crystal orientation.

Energy Dispersive X-ray spectrum (EDX) analysis of the as-synthesized SnO_2 nanoparticles

According to the EDX analysis shown in Fig. 4 and Table 2, the atomic ratio of Sn to O for all the treatments agrees with tin oxide being an *n*-type semiconductor with intrinsic carrier density primarily determined by oxygen vacancies. The EDX (Fig. 4) shows that Sn and O are present, which is in agreement with the XRD results [18].

Specific surface area and porosity

The specific surface areas of the samples were calculated by using the BET method [38]. The nanoparticles exhibit specific surface areas in the range of 18.69 m^2/g–88.31 m^2/g; pore sizes of 23.13 Å–114.93 Å; and pore volumes of 0.01 cm^3/g–0.25 cm^3/g (see Table 1. The corresponding N_2 adsorption-desorption isotherms are given in Fig. 5. The relatively high specific area of the 2.5 nm particles is due to their high surface to volume ratio as compare to the 11.5 nm nanoparticles.

Electrochemical characterization of the obtained SnO_2 nanoparticles

From the Fig. 6, it can be observed that the current under the curve increased with the increasing scan rate and this was due to the reaction time being shorter, and voltammetric current is increased if the reversibility is excellent [39]. Results also show two main peaks, a broad cathodic peak and anodic peaks corresponding to redox peak of Sn^{4+}/Sn^{3+}. The electron addition process for the SnO_2 semiconductor electrode can be written as [40].

$$Sn^{IV}O_2 + e^-_{(external)} + H^+_{(solution)} \rightarrow Sn^{III}O(OH^-) \quad (7)$$

From Fig. 7, the specific capacitance generally decreases with increasing scan rate. The specific decrease of capacitance with increase in scan rate can be attributed to electrolytic ions diffusing and migrating into the active materials at low scan rates. At high scan rates, the diffusion effect, limiting the migration of the electrolytic ions, causes some active surface areas to become inaccessible for charge storage [41].

Specific capacitance of the nanoparticles was calculated from the cyclic voltammetry (CV) curves in Fig. 6 using the following equation:

$$C_s = \frac{i}{sm} \quad (8)$$

where C_s is the specific capacitance, i is the average cathodic current, s is the scan rate and m is the mass of the electrode. It is reported that the factors affecting the capacitance are particle sizes and electro-chemical conditions, some of which are type of electrolyte, concentration of electrolyte and scan rate. Some other factors affecting the capacitance are surface activation under the electrochemical conditions, oxygen content on the surface, surface oxides and lattice defects resulting from the method of preparation [39]. The highest capacitance recorded for the SnO_2 nanoparticles was estimated to be 1.6F/g at a scan rate of 5 mV/s. The low values of capacitance recorded could be attributed to low conductivity of the SnO_2 nanoparticles, which is evident from the high internal resistance noticed in Fig. 7. The observed specific capacitance values are comparable with reported values of SnO_2 [41].

It can also be seen that samples with AOT (SAA and SCA) as the surfactant have higher capacitance than samples with CTAB (SAT and SCT) as the surfactant and samples without surfactant addition (SA and SC). This could be attributed to the fact that for samples prepared with CTAB there was agglomeration of particles, hence the porosity decreased as compared with samples prepared with AOT. This is confirmed by the SEM micrographs from Fig. 2. Enhanced porosity allows for more electrolyte penetration and hence increases charge storage [43]. Although the average crystallite size for sample SA was smaller and as such had a larger surface area compared to the other samples

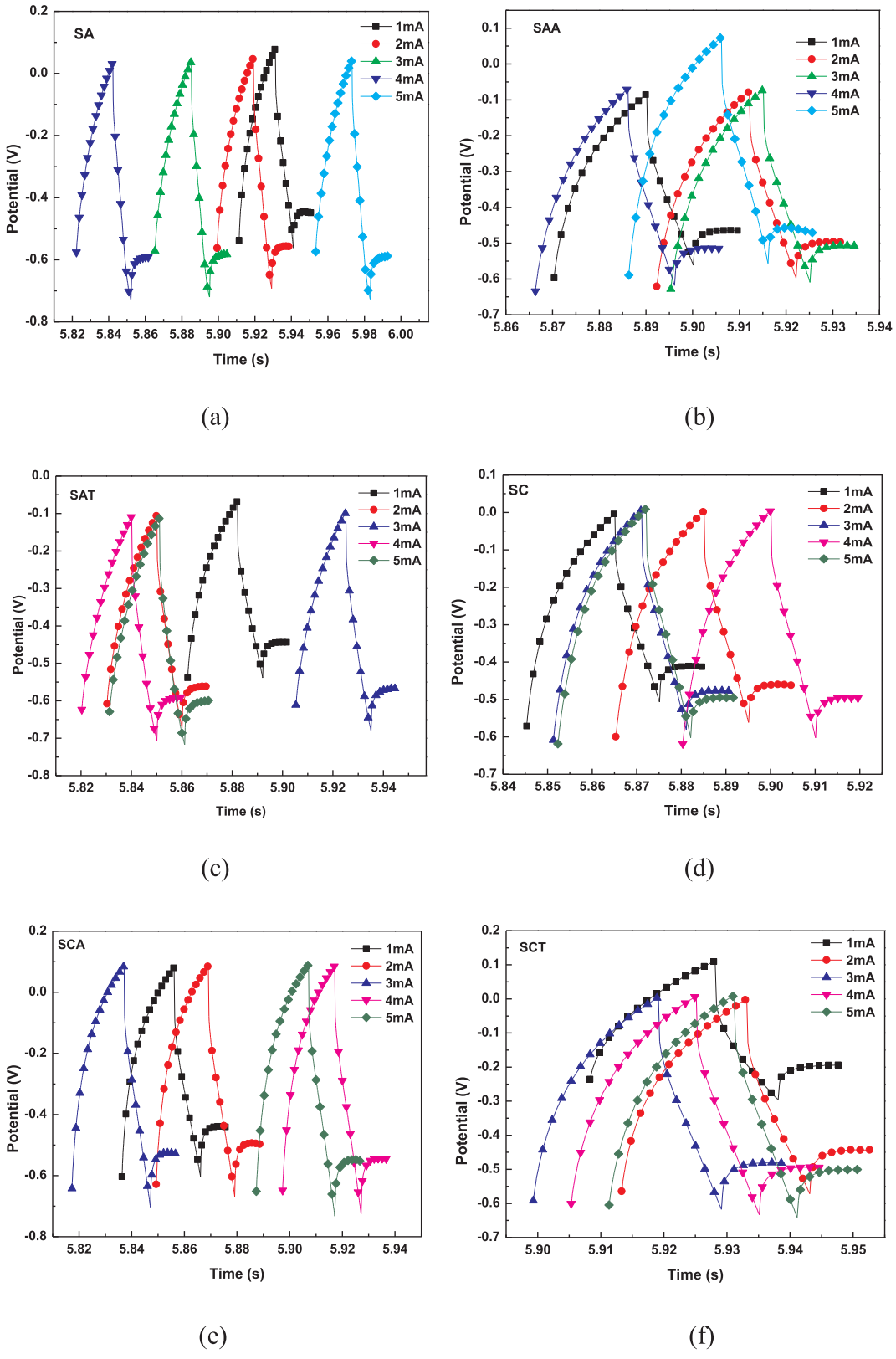

Fig. 8. Constant Current Charge-Discharge profile of the SnO_2 nanoparticles at different current densities – (a) SA; (b) SAA; (c) SAT; (d) SC; (e) SCA; (f) SCT.

Table 1, it still had a lower capacitance value recorded. This could be attributed to the fact that there was less electro active surface for the transfer of electrons and diffusion of ions [44]. Since not all the specific surface area is electrochemically accessible when the material is in contact with an electrolyte, the measured capacitance of various materials does not linearly increase with increasing specific surface area. The pore size of the electrode material plays an important role in the electrochemical active surface area. In addition, the intrinsic electrical resistance of the material may increase because the bonded heteroatom (O) possesses higher reactivity, resulting in barriers to electron

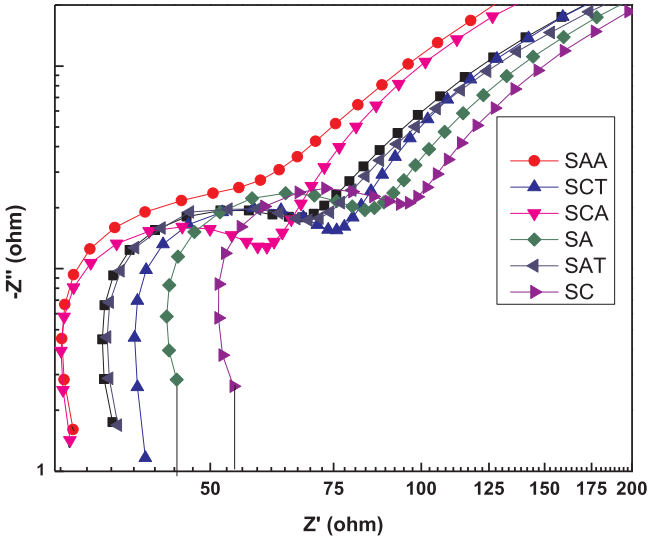

Fig. 9. The Nyquist plot for the as-synthesized SnO_2 nanoparticles.

transfer [45].

Fig. 8 compares the charge-discharge curves of the SnO_2 particles at different currents. They all show nonlinear behaviour, demonstrating the redox process of the SnO_2 particles. This is also in agreement with the cyclic voltammogram in Fig. 6. The efficiencies Ƞ of the SnO_2 electrode material were estimated from the Constant Current Charge-Discharge (CCCD) plots in Fig. 8 using the equation:

$$\eta = \frac{t_D}{t_C} \tag{9}$$

where t_D and t_C are the discharge and charge durations (s).

The relatively low energy efficiencies could essentially be attributed to the low charges storage capacity of the SnO_2 electrodes due to their high internal resistance (Fig. 9).

Fig. 9 shows the Nyquist plot, which represents the real and imaginary parts of the impedance in a sample. The x-axis intercept in the high frequency region corresponds to the resistance of the electrolyte solution (R_s), which is also referred to as the equivalent series resistance (ESR), which consists of the resistance of the aqueous electrolyte, the intrinsic resistance of the SnO_2 electrode, and the contact resistance at the electrode. The impedance spectra usually show a single semicircle in the high frequency region and a nearly vertical line in the low frequency region for a supercapacitor, which indicates that the electrode process is controlled by electrochemical reaction at high frequencies and by mass transfer at low frequencies [46]. The origin of the semicircle at higher frequency range is due to ionic charge transfer resistance (R_{ct}) at the electrode–electrolyte interface. The diameter of the semi-circle along the real axis (Z_{dia}) gives the R_{ct} [47]. It is also worth mentioning that for ideal supercapacitors, the Nyquist plot should be a line perpendicular to the real axis at low frequency. It also confirms the fact that porosity affects the electrolyte interaction with the SnO_2 particles, which in turn affects the capacitance. The ESR for the samples increase accordingly as SCA (31.5 Ω) < SAA (31.85 Ω) < SE (36.3 Ω) < SAT (36.92 Ω) < SCT (40.41 Ω) < SA < SC (53.97 Ω). These values are a confirmation of the low capacitance, efficiencies and capacitance retention recorded. The reasons for this observation are the same as explained for the capacitance.

Conclusion

SnO_2 nanoparticles with average crystallite size in the range of 2 nm–10 nm were successfully synthesized with the hydrothermal technique. Samples with surfactant addition exhibited higher capacitances than samples without surfactant addition; however, samples with surfactant AOT exhibited better capacitance than samples with surfactant CTAB due to less agglomeration. This observation suggest that the addition of surfactant AOT aids in the improvement of the capacitance performance of SnO_2 nanoparticles. The general low capacitance recorded for the SnO_2 nanoparticles from the various treatments can be attributed to the low conductivity of SnO_2.

The results obtained indicates that Sodium borohydride acts as a good reducing agent in producing SnO_2 particles with good crystallinity, high surface area and good pore structure for supercapacitor electrode material than Urea. The type of surfactant and reducing agent used also influenced the particle size and the morphology, which in turn influenced the capacitance of the SnO_2 nanoparticles.

Acknowledgement

The authors acknowledge support from the University of Ghana BANGA-Africa programme, the African Materials Science and Engineering Network and the Regional Initiative on Science and Education.

References

[1] Cheng Q, Tang J, Ma J, Zhang H, Shinya N, Qin LC. Graphene and nanostructured MnO_2 composite electrodes for supercapacitors. Carbon 2011;49(9):2917–25.
[2] Hwang SW, Hyun SH. Synthesis and characterization of tin oxide/carbon aerogel composite electrodes for electrochemical supercapacitors. J Pow Sourc 2007;172(1):451–9.
[3] Zhang YX, Huang M, Li F, Wen ZQ. Controlled synthesis of hierarchical CuO nanostructures for electrochemical capacitor electrodes. Int J Electrochem Sci 2013;8:8645–61.
[4] Bello A, Fashedemi OO, Lekitima JN, Fabiane M, Dodoo-Arhin D, Ozoemena KI, Gogotsi Y, Charlie Johnson AT, Manyala N. High-performance symmetric electrochemical capacitor based on graphene foam and nanostructured manganese oxide. AIP Adv 2013;3(8):082118.
[5] Bello A, Manyala N, Barzegar F, Khaleed AA, Momodu DY, Dangbegnon JK. Renewable pine cone biomass derived carbon materials for supercapacitor application. RSC Adv 2016;6(3):1800–9.
[6] Hu CC, Chang KH, Wang CC. Two-step hydrothermal synthesis of Ru–Sn oxide composites for electrochemical supercapacitors. Electrochimica Acta 2007;52(13):4411–8.
[7] Jayalakshmi M, Balasubramanian K. Simple capacitors to supercapacitors-an overview. Int J Electrochem Sci 2008;3(11):1196–217.
[8] Wan W, Li Y, Ren X, Zhao Y, Gao F, Zhao H. 2D SnO_2 Nanosheets: Synthesis, Characterization, Structures, and Excellent Sensing Performance to Ethylene Glycol. Nanomaterials 2018;8:112.
[9] Chen F, Shi Z, Liu M. Preparation of mesoporous SnO_2–SiO_2 composite as electrodes for lithium batteries. Chem Commun 2000;21:2095–6.
[10] Christians JA, Schulz P, Tinkham JS, Schloemer TH, Harvey SP, Tremolet de Villers BJ, Sellinger A, Berry JJ, Luther JM. Tailored interfaces of unencapsulated perovskite solar cells for > 1,000 hour operational stability. Nat Energy 2018;3(1):68.
[11] Zhang F, Lian Y, Gu M, Yu J, Tang TB. Static and Dynamic Disorder in Metastable Phases of Tin Oxide. J Phys Chem C 2017;121(29):16006–11.
[12] Li Z, Shen W, Zhang X, Fang L, Zu X. Controllable growth of SnO_2 nanoparticles by citric acid assisted hydrothermal process. Colloid Surface A 2008;327:17.
[13] Liu C, Li G-P, Cao X, Shu Y-C, Hu Y. Integrated process of large-scale and size-controlled SnO_2 nanoparticles by hydrothermal method. Trans Nonferrous Met Soc 2013;23:725–30.
[14] Bargougui R, Oueslati A, Schmerber G, Ulhaq-Bouillet C, Colis S, Hlel F, Ammar S, Dinia A. Structural, optical and electrical properties of Zn-doped SnO_2 nanoparticles synthesized by the co-precipitation technique. J Mater Sci Mater Electron 2014;25:2066.
[15] Sun JB, Sun P, Zhang DL, Xu J, Liang XS, Liu FM, Lu GY. Growth of SnO_2 nanowire arrays by ultrasonic spray pyrolysis and their gas sensing performance. RSC Adv 2014;4:43429–35.
[16] Müller R, Hernandez-ramirez F, Shen H, Du HC, Mader W, Mathur S. Influence of precursor chemistry on morphology and composition of CVD-grown SnO_2 nanowires. Chem Mater 2012;24:4028–35.
[17] Chen D, Gao L. Facile synthesis of single-crystal tin oxide nanorods with tunable dimensions via hydrothermal process. Chem Phys Lett 2004;398(1):201–6.
[18] Chen D, Gao L. Novel synthesis of well-dispersed crystalline SnO_2 nanoparticles by water-in-oil microemulsion-assisted hydrothermal process. J Coll Inter Sci 2004;279:137–42.
[19] Gnanam S, Rajendran V. Anionic, cationic and nonionic surfactants-assisted hydrothermal synthesis of tin oxide nanoparticles and their photoluminescence property. Digest J Nano Mater Biostruct 2010;5(2):623.
[20] Black DR, Windover D, Albert Henins DG, Filliben J, James PC. Standard Reference Material 640d for X-Ray Metrology. Natl Inst Stand Technol Gaithersburg, MD, 20899; 2010.
[21] Caglioti G, Paoletti A, Ricci FP. Choice of collimators for a crystal spectrometer for

neutron diffraction. Nucl Instr Meth 1958;3:223.
[22] Scardi P, Leoni M. Whole powder pattern modelling. Acta Cryst 2002;A58(190):1–18.
[23] Leoni M, Confente T, Scardi P. PM2K: a flexible program implementing whole powder pattern modelling. Z Krist Suppl 2006;23:249.
[24] Boran F, Çetinkaya S, Şahin M. Effect of surfactant types on the size of tin oxide nanoparticles. Acta Physica Polonica A 2017;132:546–8.
[25] Rani B, Punniyakoti S, Sahu NK. Polyol asserted hydrothermal synthesis of SnO_2 nanoparticles for the fast adsorption and photocatalytic degradation of methylene blue cationic dye. New J Chem 2018;42:943–54.
[26] Jiang L, Sun G, Zhou Z, Sun S, Wanget Q. Size-controllable synthesis of monodispersed SnO_2 nanoparticles and application in electrocatalysts. J Phys Chem B 2005;109(18):8774–8.
[27] Zhang J, Gao L. Synthesis and characterization of nanocrystalline tin oxide by sol-gel method. J Sol State Chem 2004;177(4):1425–30.
[28] Beller M, Fischer H, Kühlein K, Reisinger CP, Herrmann W. First palladium-catalyzed Heck reactions with efficient colloidal catalyst systems. J Organometallic Chem 1996;520(1):257–9.
[29] Song KC, Kang Y. Preparation of high surface area tin oxide powders by a homogeneous precipitation method. Mater Lett 2000;42(5):283–9.
[30] Özer MO, Suvaci E, Dogan A. Formation mechanism of nanosized tin oxide (SnO_2) powder during hydrothermal synthesis. Anadolu University J Sci Technol–A Appl Sci Eng 2011;12(1):25–36.
[31] Sun YF, Liu SB, Meng FL, Liu JY, Jin Z, Kong LT, Liu JH. Metal oxide nanostructures and their gas sensing properties: a review. Sensors 2012;12(3):2610–31.
[32] Jain K, Shrivastava A, Rashmi R. Synthesis and controlling the morphology of SnO_2 nanocrystals via Hydrothermal treatment. ECS Trans 2006;1(21):1–7.
[33] Gnanam S, Rajendran V. Anionic, cationic and nonionic surfactants-assisted hydrothermal synthesis of tin oxide nanoparticles and their photoluminescence property. Digest J Nano Mater Biostruct 2010;5(2):623.
[34] Tan L, Wang L, Wang Y. Hydrothermal synthesis of SnO_2 nanostructures with different morphologies and their optical properties. J. Nanomat. 2011;2011(23):1–10.
[35] Blessi S, Sonia MML, Vijayalakshmi S, Pauline S. Preparation and characterization of SnO_2 nanoparticles by hydrothermal method. Int J ChemTech Res 2014;6(3):2153–5.
[36] Talouki MA, Ghorbani M. Synthesis and Morphology characterization of SnO_2 nanoparticles by hydrothermal method. Int J Bio-Inorg Hybr Nanomater 2017;6(1):29–32.
[37] Kumar S, Aswal V. Tuning of nanoparticle–surfactant interactions in aqueous system. J Phy: Conden Matt 2010;23(3):035101.
[38] Lowell S, Shields JE. Powder surface area and porosity. 3rd Ed. New York: Chapman and Hall; 1991. p. 19–25.
[39] Channu VSR, Holze R, Wicker Sr SA. Synthesis and characterization of (Ru-Sn)O2 nanoparticles for supercapacitors. Mat Sci Appl 2011;2(9):1175.
[40] Venugopal N, Saiprakash PK. A study on the effect of nanosized tin oxide on the electrochemical performance of nanosized nickel hydroxide in alkali solution. J Exp Nano 2013;8(5):684–93.
[41] Li H, Yu MH, Wang FX, Liu P, Liang Y, Xiao J. Amorphous nickel hydroxide nanospheres with ultrahigh capacitance and energy density as electrochemical pseudocapacitor materials. Nat Comm 2013;4:1894.
[43] Nwanya AC, Obi D, Ozeomena KI, Osuji RU. Facile synthesis of nanosheet-like CuO film and its potential application as a high-performance pseudocapacitor electrode. Electrochimica Acta 2016;198:220–30.
[44] Sun YF, Liu SB, Meng FL, Liu JY, Jin Z, Kong LT. Metal oxide nanostructures and their gas sensing properties: a review. Sensors 2012;12(3):2610–31.
[45] Wang G, Zhang L, Zhang J. A review of electrode materials for electrochemical supercapacitors. Chem Soc Rev 2012;41(2):797–828.
[46] Song KC, Kang Y. Preparation of high surface area tin oxide powders by a homogeneous precipitation method. Mat Lett 2000;42(5):283–9.
[47] Yang D. Application of nanocomposites for supercapacitors: characteristics and properties, nanocomposites – new trends and developments. In: Ebrahimi Farzad, editor. InTech. 2012. p. 20–55. http://dx.doi.org/10.5772/50409.